OPEN ACCESS



Presupernova Neutrinos: Directional Sensitivity and Prospects for Progenitor Identification

Mainak Mukhopadhyay ¹, Cecilia Lunardini ¹, F. X. Timmes ^{2,3}, and Kai Zuber ⁴, Department of Physics, Arizona State University, Tempe, AZ 85287, USA ² School of Earth and Space Exploration, Arizona State University, Tempe, AZ 85287, USA ³ Joint Institute for Nuclear Astrophysics—Center for the Evolution of the Elements, USA ⁴ Institute für Kern- und Teilchenphysik, TU Dresden, D-01069 Dresden, Germany Received 2020 April 5; revised 2020 May 23; accepted 2020 June 3; published 2020 August 25

Abstract

We explore the potential of current and future liquid scintillator neutrino detectors of $\mathcal{O}(10)$ kt mass to localize a presupernova neutrino signal in the sky. In the hours preceding the core collapse of a nearby star (at distance $D \lesssim 1 \,\mathrm{kpc}$), tens to hundreds of inverse beta decay events will be recorded, and their reconstructed topology in the detector can be used to estimate the direction to the star. Although the directionality of inverse beta decay is weak ($\sim 8\%$ forward—backward asymmetry for currently available liquid scintillators), we find that for a fiducial signal of 200 events (which is realistic for Betelgeuse), a positional error of $\sim 60^\circ$ can be achieved, resulting in the possibility to narrow the list of potential stellar candidates to less than 10, typically. For a configuration with improved forward—backward asymmetry ($\sim 40\%$, as expected for a lithium-loaded liquid scintillator), the angular sensitivity improves to $\sim 15^\circ$, and—when a distance upper limit is obtained from the overall event rate—it is in principle possible to uniquely identify the progenitor star. Any localization information accompanying an early supernova alert will be useful to multimessenger observations and to particle physics tests using collapsing stars.

Unified Astronomy Thesaurus concepts: Neutrino astronomy (1100); Supernova neutrinos (1666); Neutrino telescopes (1105); High energy astrophysics (739)

1. Introduction

Over the next decade, neutrino astronomy will probe the rich astrophysics of neutrino production in the sky. In addition to neutrinos from the Sun (Borexino Collaboration et al. 2018), core collapse supernova bursts (e.g., SN 1987A, Alekseev et al. 1987; Bionta et al. 1987; Hirata et al. 1987, 1988), and relativistic jets (e.g., blazar TXS 0506+056, IceCube Collaboration et al. 2018a, 2018b), technological improvements in detector masses, energy resolution, and background abatement will allow us to observe new signals from different stages of the lifecycle of stars, in particular, presupernova neutrinos (Odrzywolek et al. 2004a), the diffuse supernova neutrino background (Bisnovatyi-Kogan & Seidov 1984; Krauss et al. 1984), and neutrinos from matter-rich binary mergers (Kyutoku & Kashiyama 2018; Lin & Lunardini 2020). Ultimately, the goal will be to test neutrino production across the entire Hertzsprung–Russell diagram (Farag et al. 2020).

Presupernova neutrinos are the neutrinos of ~0.1–5 MeV energy that accompany, with increasing luminosity, the last stages of nuclear burning of a massive star in the days leading to its core collapse and final explosion as a supernova, or implosion into a black hole (a "failed" supernova). These neutrinos are produced by thermal processes—mainly pair-production—that depend on the ambient thermodynamic conditions (Fowler & Hoyle 1964; Beaudet et al. 1967; Schinder et al. 1987; Itoh et al. 1996)—and by weak reactions—mainly electron/positron captures and nuclear decays—that have a stronger dependence on the isotopic composition (Fuller et al. 1980, 1982a, 1982b, 1985; Langanke & Martínez-Pinedo 2000, 2014; Misch et al. 2018), and thus on the network of nuclear reactions that take place in the stellar interior.

Original content from this work may be used under the terms of the Creative Commons Attribution 4.0 licence. Any further distribution of this work must maintain attribution to the author(s) and the title of the work, journal citation and DOI.

Building on early calculations (Odrzywolek et al. 2004a, 2004b; Kutschera et al. 2009; Odrzywolek 2009), recent numerical simulations with state-of-the-art treatment of the nuclear processes (Kato et al. 2015, 2017; Yoshida et al. 2016; Patton et al. 2017a, 2017b; Guo et al. 2019) have shown that the presupernova neutrino flux increases dramatically, both in luminosity and in average energy, in the hours prior to the collapse, and it becomes potentially detectable when silicon burning is ignited in the core of the star. In particular, for stars within ~ 1 kpc of Earth like Betelgeuse, presupernova neutrinos will be detected at multi-kiloton neutrino detectors like the current KamLAND (see Araki et al. 2005 for a dedicated study), Borexino (Borexino Collaboration et al. 2018), Sudbury Neutrino Observatory (SNO+; Andringa et al. 2016), Daya Bay (Daya Bay Collaboration et al. 2007), and SuperKamiokande (Simpson et al. 2019), as well as the upcoming HyperKamiokande (Abe et al. 2016), Deep Underground Neutrino Experiment (DUNE; Acciarri et al. 2016), and Jiangmen Underground Neutrino Observatory (JUNO; Li 2014; An et al. 2016; Brugière 2017). Next generation dark matter detectors like XENON (Newstead et al. 2019), DARk matter WImp search with liquid xenoN (DARWIN; Aalbers et al. 2016), and Astrophysical Radiation with Ground Based Observatory (ARGO; Aalseth et al. 2018) will also observe a significant signal (Raj et al. 2020). Therefore, presupernova neutrinos are a prime target for the SuperNova Early Warning System network (SNEWS, Antonioli et al. 2004)—which does or will include the neutrino experiments mentioned above-and its multimessenger era successor SNEWS 2.0, whose mission is to provide early alerts to the astronomy and gravitational wave communities, and to the scientific community at large as well. The observation of presupernova neutrinos from an impending core collapse supernova will (i) allow numerous tests of stellar and neutrino physics, including tests of exotic physics that may

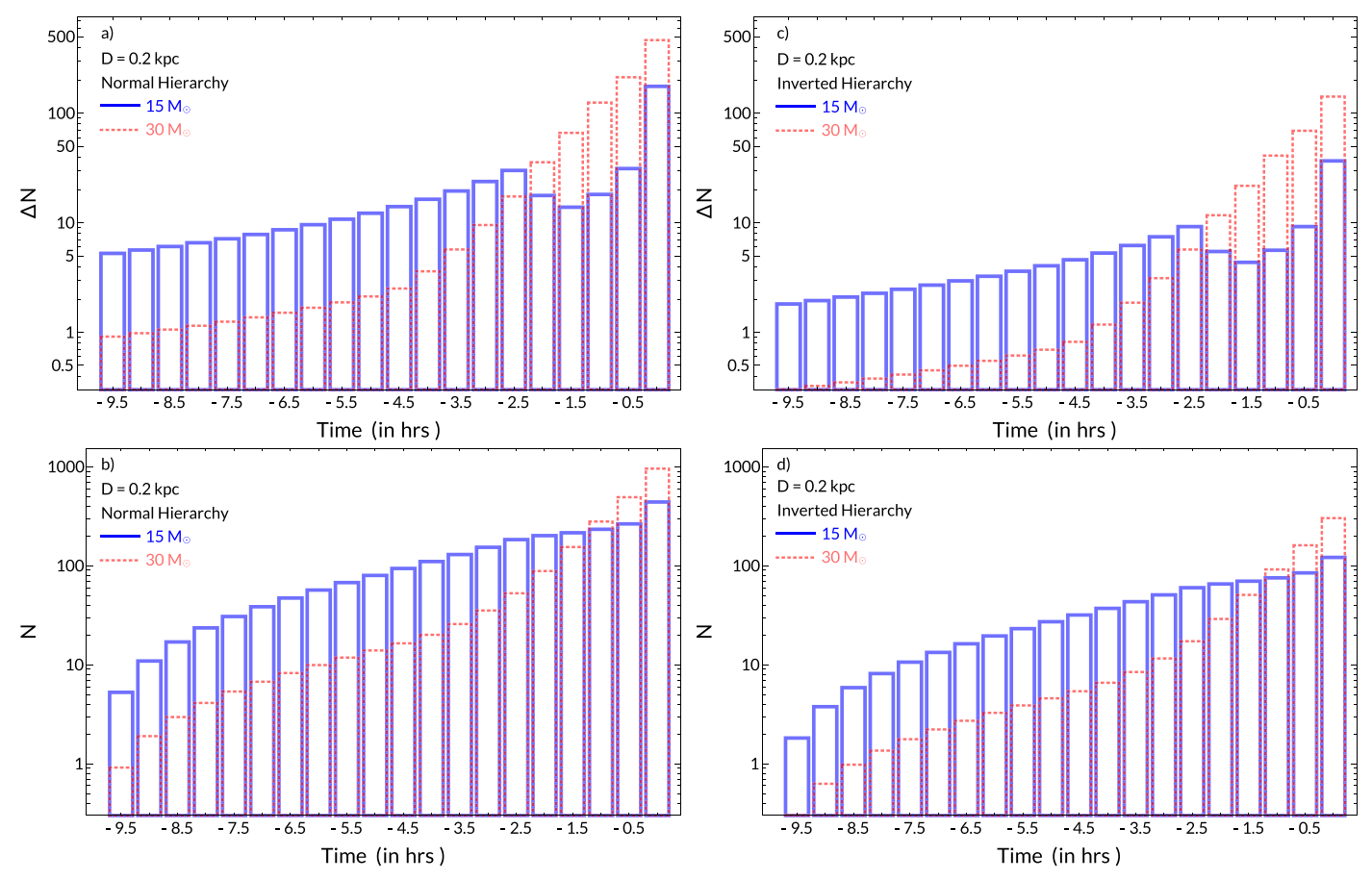


Figure 1. Top row (a) and (c): Number of presupernova neutrino events at a 17 kt liquid scintillator detector, in time bins of width $\Delta t = 0.5$ hr as a function of time before core collapse. Bottom row (b) and (d): Cumulative numbers of events in half-hour increments. Shown are the cases of a ZAMS 15 M_{\odot} (blue histogram) and a ZAMS 30 M_{\odot} (red histogram) progenitor, at a distance D = 0.2 kpc, for the normal (left column) and inverted (right column) neutrino mass hierarchy.

require pointing to the collapsing star (e.g., axion searches, see Raffelt et al. 2011); and (ii) enable a very early alert of the collapse and supernova, thus extending—perhaps crucially, especially for envelope-free stellar progenitors that tend to explode shortly after collapse—the time frame available to coordinate multimessenger observations.

In this paper, we explore presupernova neutrinos as early alerts. In particular, we focus on the question of localization: can a signal of presupernova neutrinos provide useful positional information? Can it identify the progenitor star? From a recent exploratory study (Li et al. 2020), we know that the best potential for localization is offered by inverse beta decay events at large ($\mathcal{O}(10)$ kt mass) liquid scintillator detectors, where, for optimistic presupernova flux predictions and a star like Betelgeuse (distance of 0.2 kpc), a signal can be discovered days before the collapse, and the direction to the progenitor can be determined with an $\sim 80^{\circ}$ error.

This article is the first dedicated study on the localization question for presupernova neutrinos. Using a state-of-the-art numerical model for the neutrino emission, we examine a number of questions that were not previously discussed, having to do with the diverse stellar population of nearby stars (including red and blue supergiants, of masses between $\sim \! 10$ and $\sim \! 30$ times the mass of the Sun, and clustered in certain regions of the sky) and with the rich possibilities of improving the directionality of the liquid scintillator technology in the future.

In Section 2 we discuss presupernova neutrino event rates and nearby candidates. In Section 3 we present our main results

for the angular sensitivity. In Section 4 we discuss progenitor identification, and in Section 5 we summarize our results. In the Appendix we detail the distance and mass estimates of nearby presupernova candidates.

2. Presupernova Neutrino Event Rates and Candidates

A liquid scintillator is ideal for the detection of presupernova neutrinos, through the inverse beta decay process (henceforth IBD, $\bar{\nu}_e + p \rightarrow n + e^+$) due to its low energy threshold (1.8 MeV), and its timing, energy resolution, and background discrimination performance. The expected signal from a presupernova in neutrino detectors has been presented in recent articles (e.g., Kato et al. 2015, 2017; Asakura et al. 2016; Yoshida et al. 2016; Patton et al. 2017b; Li et al. 2020).

We consider an active detector mass of 17 kt, which is expected for JUNO, with detection efficiency of unity, and we use the IBD event rates in Patton et al. (2017a, 2019). Figure 1 shows the numbers of events and cumulative numbers of events for progenitor stars of zero age main-sequence (ZAMS) masses of 15 M_{\odot} and 30 M_{\odot} (here $M_{\odot}=1.99~10^{33}$ g is the mass of the Sun) at a distance of D=0.2 kpc (representative of Betelgeuse). Results are shown for the normal and inverted hierarchy of the neutrino mass spectrum. Times are negative, being relative to the time of core collapse.

Figure 1 shows that a few hundred events are expected in the hours before core collapse. For the $15\,M_\odot$ model, the neutrino signal exceeds $\simeq 100$ events at t=-4 hr and has a characteristic

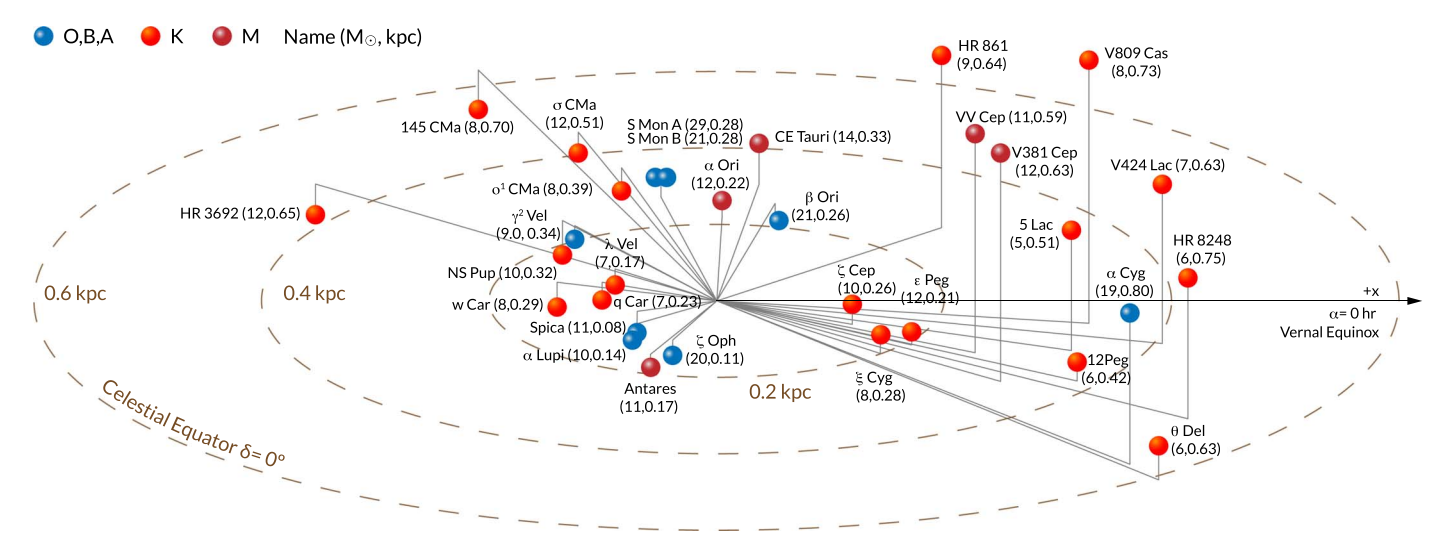


Figure 2. Illustration of nearby ($D \le 1$ kpc) core collapse supernova candidates. Each star's spectral type, name, mass, and distance is shown in labels. See Table A1 for details and references.

peak at $t \simeq -2.5$ hr, which marks the beginning of core silicon burning. For the $30\,M_\odot$ model, the neutrino signal exceeds $\simeq 100$ events at t=-2 hr. The number of events then increases steadily and rapidly, leading to a cumulative number of events that is larger than in the $15\,M_\odot$ model.

For the detector background, we follow the event rates estimated in An et al. (2016) (see also Yoshida et al. 2016) for JUNO: $r_{\rm Bkg}^{\rm on} \simeq 2.66~\rm hr^{-1}$ and $r_{\rm Bkg}^{\rm off} \simeq 0.16~\rm hr^{-1}$ in the reactor-on and reactor-off cases respectively. In addition to reactor neutrinos, other backgrounds are due, in comparable amounts (about one event per day each), to geoneutrinos, cosmogenic 8 He/ 9 Li, and accidental coincidences due to various radioactivity sources, like the natural decay chains, etc. For the latter, it is assumed that an effective muon veto will be in place, see An et al. (2016) for details. Roughly a signal is detectable if the number of events expected is at least comparable with the number of background events in the same time interval ($N \gtrsim N_{\rm bkg}$). Using the reactor-on background rate, the most conservative presupernova event rate in Figure 1, and the fact that the number of signal events scales like D^{-2} , we estimate that a presupernova can be detected to a distance $D_{\rm max} \simeq 1~\rm kpc$.

What nearby stars could possibly undergo core collapse in the next few decades? To answer this question, we compiled a new list of 31 core collapse supernova candidates; see the Appendix and Table A1. Figure 2 gives an illustration of their names, positions, distances, masses, and colors. Figure 3 shows the equatorial coordinate system positions of the same stars, colored by distance bins, in a Mollweide projection. These candidates lie near the Galactic plane, with clustering in directions associated with the Orion A molecular cloud (Großschedl et al. 2019) and the OB associations Cygnus OB2 and Carina OB1 (Lim et al. 2019). We find that for the stars in Table A1 the minimum separation (i.e., the separation of a star from its nearest neighbor in the same list) is, on average, $\langle \Delta \theta \rangle \simeq 10^\circ.4$, and that 70% of the candidate stars have $\Delta \theta \lesssim 12^\circ.8$ (see Table A2). Therefore, a sensitivity of

 $\simeq 10^{\circ}$ is desirable for complete disambiguation of the progenitor with a neutrino detector.

3. Angular Resolution and Sensitivity

Here we discuss the angular sensitivity of a liquid scintillator detector for realistic numbers of presupernova neutrino events. We consider two cases: a well tested liquid scintillator technology (henceforth LS) based on Linear AlkylBenzene, as is used in SNO+ (Andringa et al. 2016) and envisioned for JUNO; and a hypothetical setup where a Lithium compound is dissolved in the scintillator for enhanced angular sensitivity (henceforth LS-Li), as discussed for geoneutrino detection (Tanaka & Watanabe 2014). As a notation definition, let us assume that the total number of events in the detector is $N = N_S + N_{\rm Bkg}$, where N_S is the number of signal events and $N_{\rm Bkg}$ is the number of background events.

The IBD process in LS is illustrated in Figure 4. Overall, the sensitivity of this process to the direction of the incoming neutrino is moderate, with the emitted positron (neutron) momentum being slightly backward (forward)-distributed, see Beacom & Vogel (1999) and Vogel & Beacom (1999) for a detailed overview. Here, we follow the pointing method proposed and tested by the CHOOZ collaboration (Apollonio et al. 2000), which we describe briefly below.

Let us first consider a background-free signal, $N_{\rm Bkg}=0$. For each detected neutrino ν_i (i=1,2,...,N), we consider the unit vector $\hat{X}_{\rm pn}^{(i)}$ that originates at the positron annihilation location and is directed toward the neutron capture point. Let θ be the angle that $\hat{X}_{\rm pn}^{(i)}$ forms with the neutrino direction (see Figure 4). The unit vectors $\hat{X}_{\rm pn}^{(i)}$ carry directional information—albeit with some degradation due to the neutron having to thermalize by scattering events before it can be captured—and possess a slightly forward distribution. The angular distributions expected for LS and LS-Li are given by Tanaka & Watanabe (2014) (in the context of geoneutrinos) in graphical form; we find that they are well reproduced by the following functions:

$$f_{\rm LS}(\cos\theta) \simeq 0.2718 + 0.2238 \exp(0.345\cos\theta)$$

 $f_{\rm LS-Li}(\cos\theta) \simeq 0.1230 + 0.3041 \exp(1.16\cos\theta).$ (1)

⁵ Although we use detector-specific background rates, we emphasize that our results are given as a function of the forward-backward asymmetry of the data set at hand, and therefore are broadly applicable to different detector setups. See Section 3.

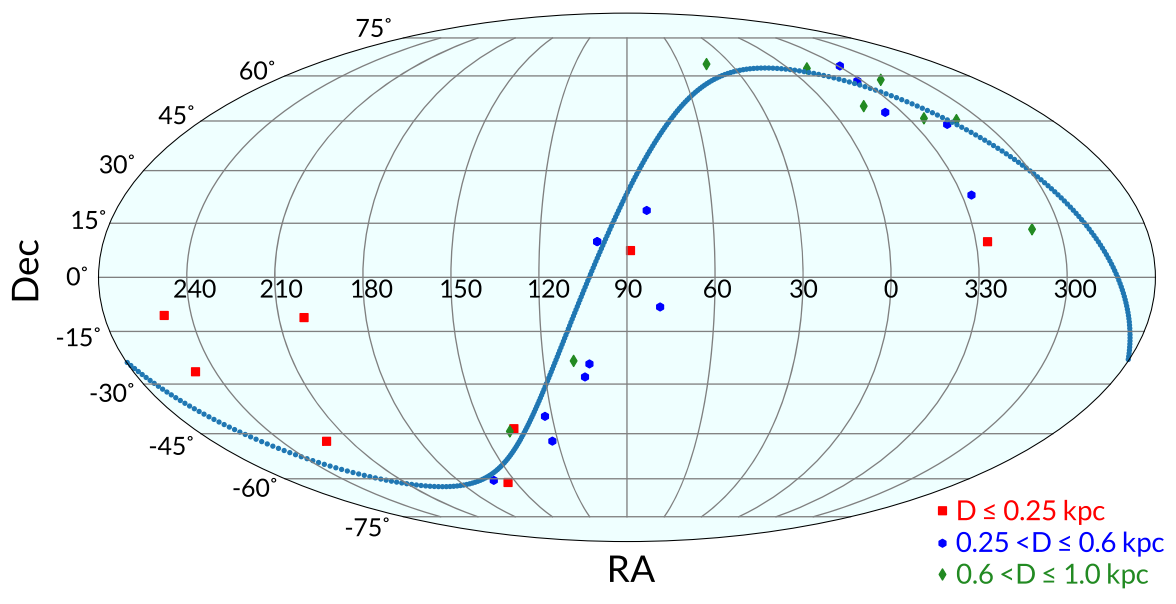


Figure 3. Mollweide projection of nearby ($D \le 1$ kpc) core collapse supernova candidates. Symbols and colors correspond to distance intervals. The dotted line indicates the Galactic plane. The red square near the center of the map is α Ori, best known as Betelgeuse.

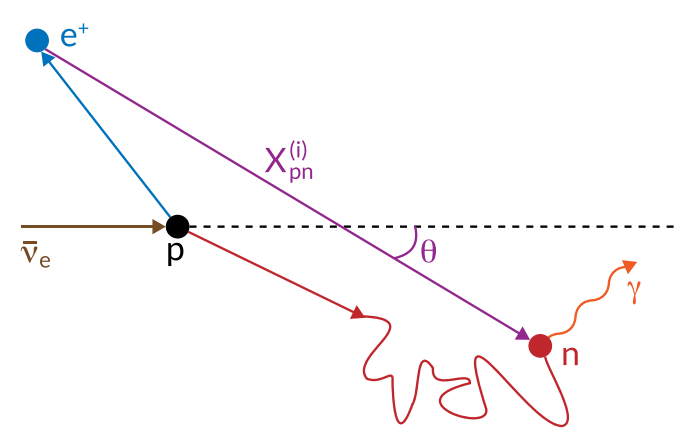


Figure 4. The geometry of inverse beta decay in liquid scintillator. Shown are the incoming antineutrino (brown), proton (black), outgoing positron and its annihilation point (blue), outgoing neutron, its subsequent scattering events and its capture point (red), and the outgoing photon (orange). The vector $X_{\rm pn}^{(i)}$ originates at the positron annihilation location and points in the direction of the neutron capture point. θ is the angle between $X_{\rm pn}^{(i)}$ and the incoming neutrino momentum.

Using these, one can find the forward—backward asymmetry, which is a measurable parameter:

$$\frac{a_0}{2} = \frac{N_F - N_B}{N_F + N_B}. (2)$$

Here N_F and N_B are the numbers of events in the forward $(\theta \leqslant \pi/2)$ and backward $(\theta > \pi/2)$ direction respectively. We obtain $a_0 \simeq 0.16$ for LS, which is consistent with the distributions shown in Apollonio et al. (2000), and $a_0 \simeq 0.78$ for LS-Li.

Let us now generalize to the case with a nonzero background, and define the signal-to-background ratio, $\alpha = N_S/N_{\rm Bkg}$. For simplicity, the background is modeled as isotropic and constant in time. Suppose that N_S , α , and a_0 are known. In this case, the total angular distribution of the N events will be a linear combination of two components, one for

the directional signal

$$N_{B,S} = \frac{N_S}{2} \left(1 - \frac{a_0}{2} \right)$$

$$N_{F,S} = \frac{N_S}{2} \left(1 + \frac{a_0}{2} \right), \tag{3}$$

and the other for the isotropic background

$$N_{B,\text{Bkg}} = \frac{N_{\text{Bkg}}}{2} \qquad N_{F,\text{Bkg}} = \frac{N_{\text{Bkg}}}{2}.$$
 (4)

The two distributions have a relative weight of α , which yields the forward–backward asymmetry as

$$\frac{a}{2} = \frac{(N_{F,S} + N_{F,Bkg}) - (N_{B,S} + N_{B,Bkg})}{(N_{F,S} + N_{F,Bkg}) + (N_{B,S} + N_{B,Bkg})}.$$
 (5)

In the small background limit, $N_{\rm Bkg} \to 0$, then $\alpha \to \infty$ and $a \to a_0$. In the large background limit $N_{\rm Bkg} \to \infty$, then $\alpha \to 0$ and $a \to 0$.

Figure 5 shows the angular distribution for different signal-to-noise ratios α (see Table 1 for the corresponding values of a). For LS the $\alpha=\infty$ curve (blue solid) is taken from Equation (1), and for LS-Li the $\alpha=\infty$ curve (red solid) is taken from Equation (1). For LS-Li, an enhancement in the directionality is achieved as a result of an improved reconstruction of the positron annihilation point and a shortening of the neutron capture range. Enhancement in the directionality decreases for LS and LS-Li as the background becomes larger.

From here on, for all cases we adopt an approximate linear distribution for the N events in the detector:

$$f(\cos \theta) = \frac{1}{2}(1 + a\cos \theta). \tag{6}$$

This form is accurate—yielding results that are commensurate with those obtained from the distributions in Figure 5—and it allows us to describe our results as functions of the varying parameter *a* in a general and transparent manner.

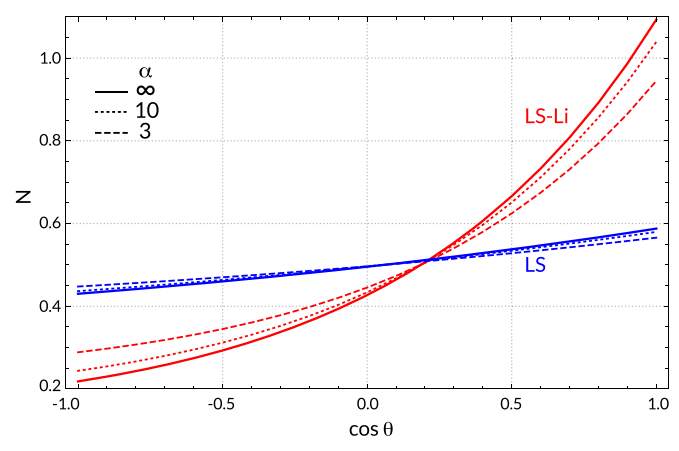


Figure 5. Normalized distributions of $\cos\theta$ for LS and LS-Li, for different values of the signal-to-background ratio, $\alpha=N_{\rm S}/N_{\rm Bkg}$ (numbers in legend). Here, $\alpha=\infty$ means the absence of background, $N_{\rm Bkg}=0$.

Table 1Values of *a* for the Curves in Figure 5

α	LS	LS-Li
∞	0.1580	0.7820
10.0	0.1418	0.7165
3.0	0.1170	0.5911

Rigorously, a depends on the neutrino energy. We investigated the uncertainty associated with treating a as a (energy-independent) constant, and found it to be negligible in the present context where larger errors are present from, for example, uncertainties associated with modeling of the presupernova neutrino event rates. In addition, the values of a used in the literature for supernova neutrinos, reactor neutrinos, and geoneutrinos (e.g., Apollonio et al. 2000; Tanaka & Watanabe 2014; Fischer et al. 2015) vary only by $\simeq 10\%-20\%$ over a wide range of energy. The values of a in Table 1 for the background-free $\alpha=\infty$ cases are used in Tanaka & Watanabe (2014) and Fischer et al. (2015) for geoneutrinos, which have an energy range ($E\simeq 2-5$ MeV) and spectrum that is similar to those of presupernova neutrinos.

3.1. Pointing to the Progenitor Location

For a signal of N IBD events in the detector from a point source on the sky, and therefore a set of unit vectors $\hat{X}_{pn}^{(i)}$ (i=1,2,...,N), an estimate of the direction to the source is given by the average vector p (Apollonio et al. 2000; Fischer et al. 2015):

$$p = \frac{1}{N} \sum_{i=1}^{N} \hat{X}_{pn}^{(i)}.$$
 (7)

This vector offers an immediate way to estimate the direction to the progenitor star in the sky. The calculation of the uncertainty in the direction is more involved (Apollonio et al. 2000), and requires examining the statistical distribution of p, as follows.

Consider a Cartesian frame of reference where the neutrino source is on the negative side of the z-axis. In the limit of very high statistics $(N \to \infty)$, the averages of the x- and y-components of the vectors $\hat{X}_{pn}^{(i)}$ vanish. The average of the z-component can be found from Equation (6), and is $\langle z \rangle = a/3$.

Thus, the mean of p is:

$$\mathbf{p}_{m} = (0, 0, |\mathbf{p}|) = (0, 0, a/3).$$
 (8)

For the linear distribution in Equation (6), the standard deviation is $\sigma = (\sqrt{3-a^2})/3 \simeq 1/\sqrt{3}$ (where the approximation introduces a relative error of the form $a^2/6$, which is negligible in the present context). For $N \gg 1$, the central limit theorem applies, and the distribution of the three components of \boldsymbol{p} are Gaussians⁶ centered at the components of \boldsymbol{p}_m , and with standard deviations $\sigma_x = \sigma_y = \sigma_z = \sigma = 1/\sqrt{3N}$. Hence, the probability distribution of the vector \boldsymbol{p} is

$$P(p_x, p_y, p_z) = \frac{1}{(2\pi\sigma^2)^{\frac{3}{2}}} \exp\left(\frac{-p_x^2 - p_y^2 - (p_z - |\mathbf{p}|)^2}{2\sigma^2}\right).$$
(9)

The angular uncertainty on the direction to the supernova progenitor is given by the angular aperture, β , of the cone around the vector \mathbf{p}_m , containing a chosen fraction of the total probability (e.g., I = 0.68 or I = 0.90):

$$\int P(p_x, p_y, p_z) dp_x dp_y dp_z = I, \qquad (10)$$

or, in spherical coordinates:

$$\int_{0}^{\infty} p^{2} dp \int_{\cos \beta}^{1} d\cos \theta \int_{0}^{2\pi} d\phi \ P(p_{x}, p_{y}, p_{z}) = I.$$
 (11)

The latter form reduces to:

$$\frac{1}{2}[1 + \operatorname{Erf}(k) - \cos\beta \exp(-k^2 \sin^2\beta) \times (1 + \operatorname{Erf}(k \cos\beta))] = I,$$
(12)

where $k = \sqrt{3N/2} |\mathbf{p}| = a\sqrt{N/6}$, and the error function is $\mathrm{Erf}(z) = 2/\sqrt{\pi} \int_0^z \exp(-t^2) dt$.

For a fixed value of I, Equation (12) can be solved numerically to find $\beta = \beta(k, I)$, and therefore to reveal the dependence of β on N and a. Figure 6 shows the dependence of β on N, for two confidence levels (C.L.). The figure illustrates the (expected) poor performance of LS: we have $\beta \simeq 70^{\circ}$ at 68% C.L. and N = 100, improving to $\beta \simeq 40^{\circ}$ at N = 500. For the same C.L. and values of N, LS-Li would allow an improvement in the error by nearly a factor of 4, giving $\beta \simeq 18^{\circ}$ and $\beta \simeq 10^{\circ}$ in the two cases respectively. The degree of improvement in performance with increasing a is shown in Figure 7, where N = 200 is kept fixed.

In the case of isotropic background the mean vector, p_m , still points in the direction of the progenitor star. That is no longer true in the general case of anisotropic background, which would introduce a systematic shift in the direction of p_m . A naive estimate for a point-like source of background gives an (average) shift in direction by an angle $\delta \lesssim N_{\rm Bkg}/N_{\rm S}$ (valid if $N_{\rm Bkg} \ll N_{\rm S}$ and independent of a), corresponding to $\delta \lesssim 4^{\circ} - 10^{\circ}$ for parameters typical of Betelgeuse (see Table 2). A comparison

This statement (and therefore Equation (9)) is only valid in the assumed frame of reference, which is centered at the detector, with the neutrino source being on the z-axis. In a generic frame of reference, the three components of p are not statistically independent, and their probability distribution takes a more complicated form.

 Table 2

 Parameters and Results for Betelgeuse, Figure 8, Left Panels

						LS			LS-Li	
Time to CC	N_{Total}	$N_{\rm Signal}$	$N_{ m Bkg}$	α	а	68% C.L.	90% C.L.	а	68% C.L.	90% C.L.
4.0 hours	93	78	15	5.20	0.1308	78.43°	116.17°	0.6610	23.24°	33.98°
1.0 hour	193	170	23	7.39	0.1374	63.92°	98.42°	0.6942	15.47°	22.26°
2 minutes	314	289	25	11.56	0.1435	52.72°	81.79°	0.7254	11.63°	16.67°

Note. The angular errors at a given confidence level (C.L.) are in degrees.

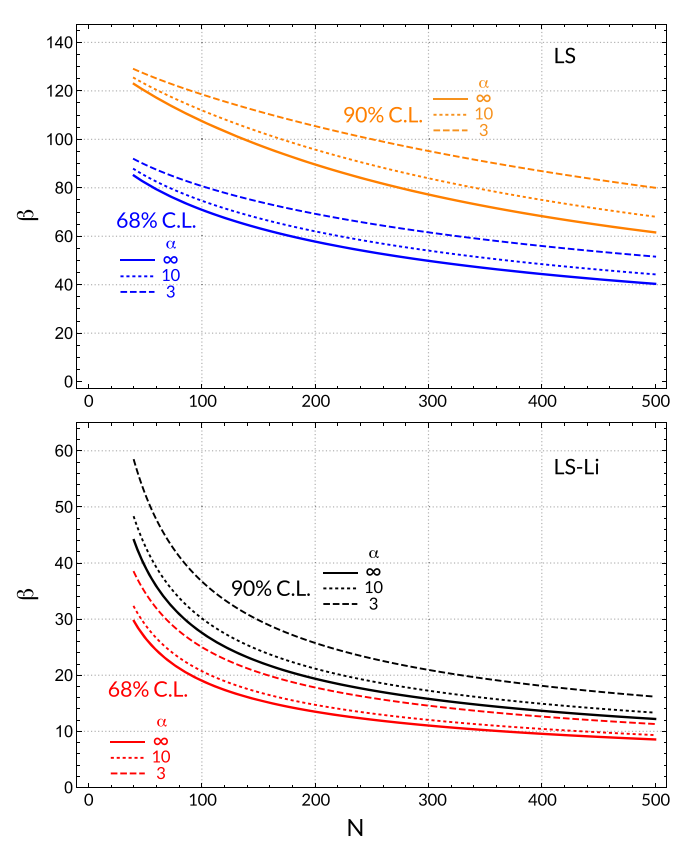


Figure 6. The angular uncertainty, β , as a function of the number of events, for LS and LS-Li, two different confidence levels, and three values of the signal-to-background ratio, α (see figure legend).

with the typical values of β indicates that the shift is probably negligible for LS ($\beta \gg \delta$, typically) but might have to be considered for LS-Li. A more accurate estimate of δ depends on site-specific information and is beyond the scope of the present paper.

Another source of potential uncertainty is in the site-specific number of accidental coincidences in the detector (e.g., a coincidence between a positron from a cosmic muon decay and a neutron capture from a different process). Although here we assume a strong muon veto (An et al. 2016), the actual performance of the veto in a realistic setting may be different and contribute to larger background levels that would negatively affect the presupernova localization. See Cao & Wang (2017) and references therein for technical information on realistic veto designs and their expected performance.

4. Progenitor Identification

Attempts at progenitor identification will involve a complex interplay of different information from different channels.

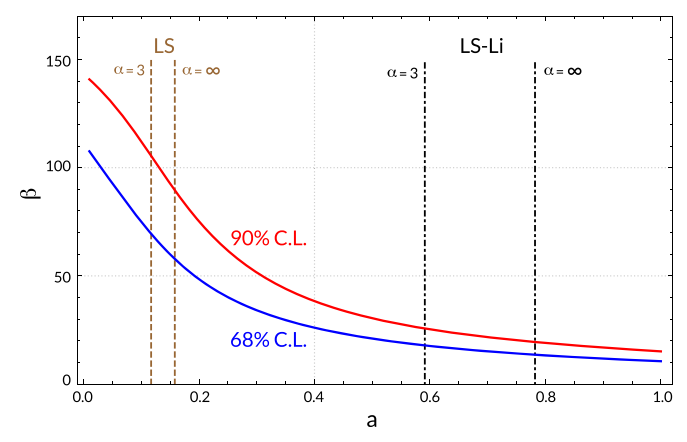


Figure 7. The angular uncertainty, β , as a function of the forward-backward asymmetry, a, for two different confidence levels (see figure legend) and fixed number of events, N=200. The vertical lines indicate the values of a corresponding to $\alpha=\infty$, 3 for LS (dashed lines) and LS-Li (dotted-dashed), see Table 1

Here, we discuss a plausible, although simplified, scenario where two essential elements are combined: (i) pointing information from a single liquid scintillator detector, using the method in Section 3; and (ii) a rough estimate of the distance to the star, from the comparison of the signal with models. Both these indicators will evolve with time over the duration of the presupernova signal, with the list of plausible candidates becoming shorter as higher statistics are collected in the detector. We emphasize that the goal here is not necessarily to reduce to a single star; even reducing the list to a few stars (3 or 4, for example) can be useful to the gravitational wave and electromagnetic astronomy communities.

Consider the two case studies shown in Figure 8 and detailed in Tables 2 and 3. The left column refers to Betelgeuse and the right column to Antares, both with a time distribution of IBD events as in Figure 1 for $15 M_{\odot}$. The three panels show how the 68% and 90% C.L. angular errors decrease with time, leading to a progressively more accurate estimate of the position.⁸

For the case of LS, at $t=-1\,\mathrm{hr}$ precollapse, as many as $\sim\!10$ progenitor stars are within the angular error cone, with only a minimal improvement at later times. Therefore, the identification of the progenitor cannot be achieved using the angular information alone. It might be possible, however, in the presence of a rough distance estimation from the event rate in the detector. In both examples, a possible upper limit of

Circumstances that could further narrow the list of candidate stars include unusual electromagnetic activity from a candidate in the weeks or days preceding the signal, improving the distance estimate using data from multiple detectors, etc.

In a realistic situation, the center of the angular error cone would be shifted away from the true position of the progenitor star by a statistical fluctuation. This effect is not included here.

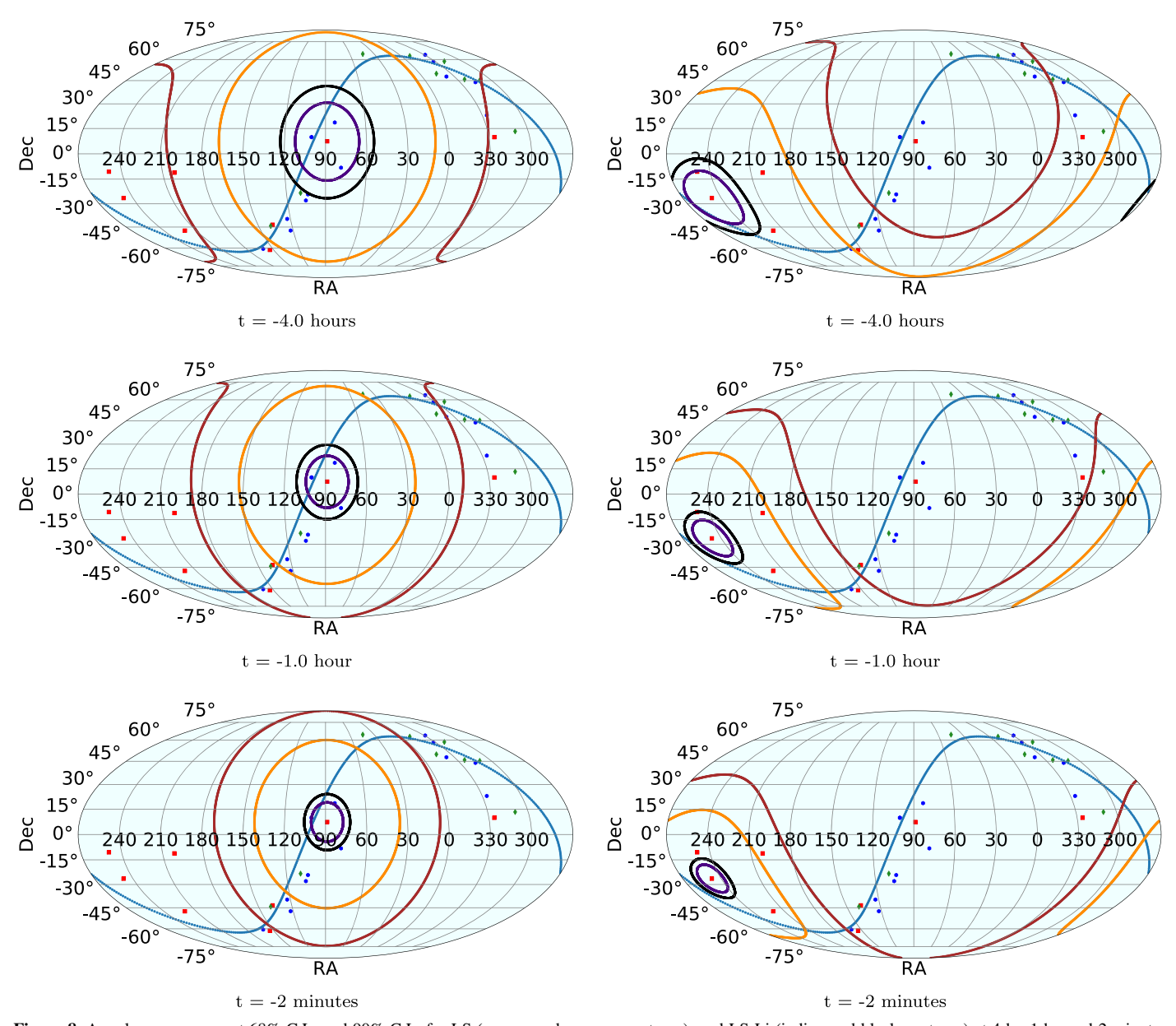


Figure 8. Angular error cones at 68% C.L. and 90% C.L. for LS (orange and maroon contours), and LS-Li (indigo and black contours) at 4 hr, 1 hr, and 2 minutes prior to the core collapse. The left panels correspond to Betelgeuse (D = 0.222 kpc, $M \simeq 15M_{\odot}$); the right panels to Antares (D = 0.169 kpc, $M \simeq 15M_{\odot}$). The presence of background is considered in all cases according to An et al. (2016). The number of events is based on the model by Patton et al. (2017b).

 Table 3

 Parameters and Results for Antares, Figure 8, Right Panels

						LS			LS-Li	
Time to CC	$N_{ m Total}$	$N_{\rm Signal}$	$N_{ m Bkg}$	α	а	68% C.L.	90% C.L.	a	68% C.L.	90% C.L.
4.0 hours	161	146	15	9.73	0.1414	66.27°	101.59°	0.7147	16.44°	23.70°
1.0 hour	333	310	23	13.48	0.1452	51.11°	79.24°	0.7337	11.16°	15.98°
2 minutes	543	518	25	20.72	0.1488	41.02°	62.70°	0.7519	8.54°	12.19°

D < 0.25 kpc (red squares in Figure 8, also see Figure 3) results in a single presupernova being favored. For LS-Li, the angular information alone is sufficient to favor 3–4 stars as likely progenitors already \sim 4 hr precollapse. At t=-1 hr, a single progenitor can be identified in the case of Antares.

A less fortunate scenario is shown in the left panels in Figure 9 (details in Table 4) for σ Canis Majoris (distance

 $D=0.513~{\rm kpc}$). The number of events was calculated according to the $15M_{\odot}$ model in Figure 1. The lower signal statistics (the number of events barely reaches 60), and the larger relative importance of the background result in a decreased angular sensitivity. We find that LS will only eliminate roughly half of the sky if we use the 68% C.L. error cone. When combined with an approximate distance estimate,

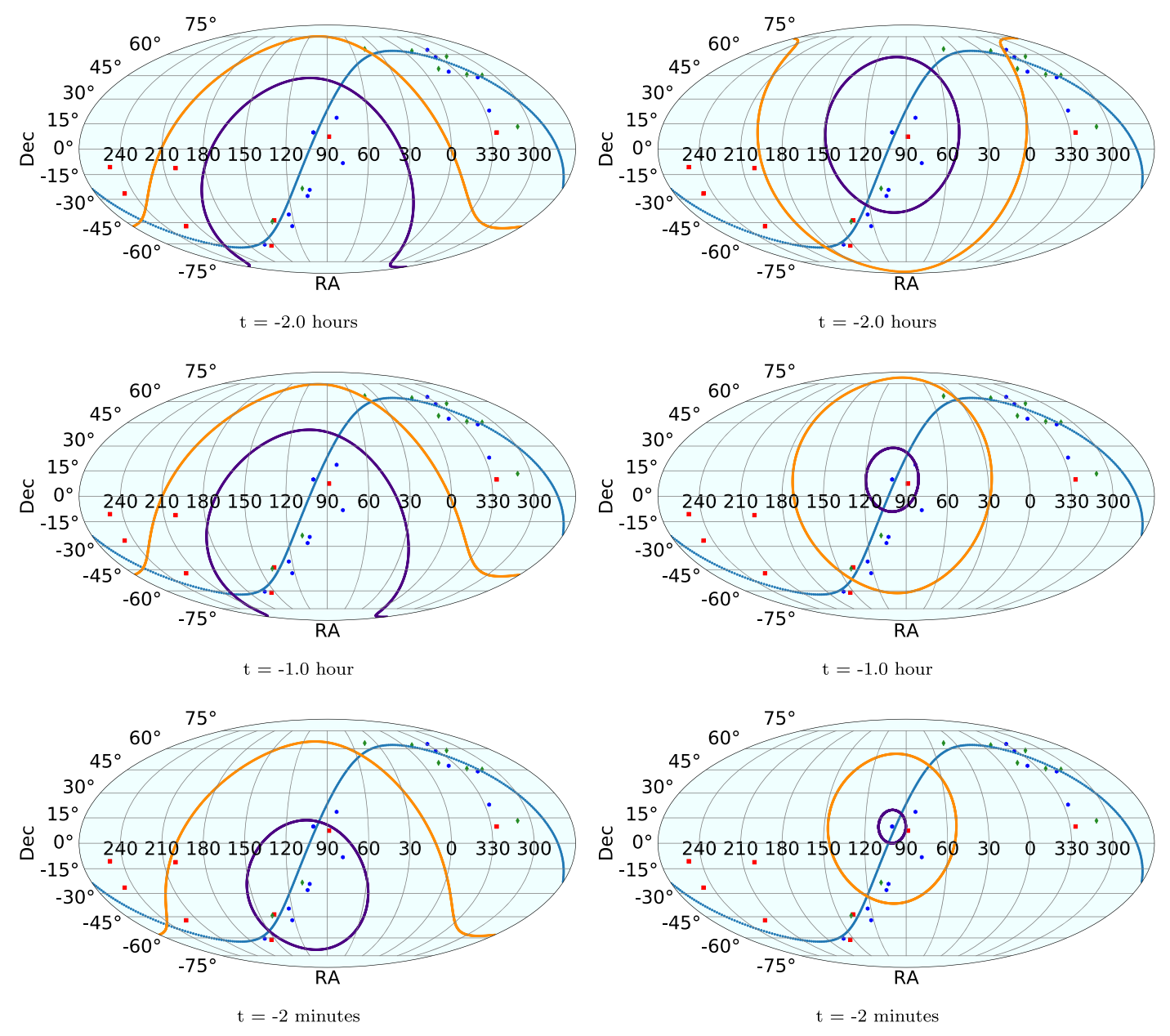


Figure 9. Same as Figure 8, but for σ Canis Majoris (left panels, D=0.513 kpc, $M\simeq 15M_{\odot}$) and S Monocerotis A (right panels, D=0.282 kpc, $M\simeq 30M_{\odot}$). Only 68% C.L. contours are shown here, for LS (orange) and LS-Li (indigo).

 Table 4

 Parameters and Results for σ Canis Majoris, Figure 9, Left Panels

						LS	I	_S-Li
Time to CC	$N_{ m Total}$	$N_{ m Signal}$	$N_{ m Bkg}$	α	a	68 % C.L.	a	68 % C.L.
2.0 hours	31	11	20	0.55	0.0553	103.28°	0.2797	71.43°
1.0 hour	36	13	23	0.56	0.0560	102.54°	0.2829	68.32°
2 minutes	58	33	25	1.32	0.0887	93.56°	0.4484	41.57°

this coarse angular information might lead to identifying $\sim \! \! 10$ stars as potential candidates. With LS-Li, the list of candidates might be slightly shorter but a unique identification would be very unlikely, even immediately before collapse.

A $30 M_{\odot}$ case is represented by the right panels in Figure 9 (and detailed in Table 5) for S Monocerotis A (distance D = 0.282 kpc). An hour prior to the collapse $\simeq 120$ events are

expected, allowing LS to shorten the progenitor list to \simeq 12 stars within the error cone at 68% C.L. Whereas, LS-Li narrows the progenitor list down to \simeq 3 stars with the same C.L. one hour prior to the collapse. When combined with a rough distance estimate, the progenitor might be successfully identified.

In conclusion of this section, let us elaborate on the potential of estimating the distance to the star by comparing the observed

Table 5
Parameters and Results for S Monocerotis A, Figure 9, Right Panels

						LS		LS-Li		
Time to CC	$N_{ m Total}$	$N_{ m Signal}$	$N_{ m Bkg}$	α	a	68 % C.L.	a	68 % C.L.		
2.0 hours	44	24	20	1.20	0.0850	96.53°	0.4300	48.26°		
1.0 hour	141	118	23	5.13	0.1305	71.60°	0.6596	19.00°		
2 minutes	420	395	25	15.80	0.1466	46.28°	0.7413	9.84°		

neutrino event rate with models. The accuracy of such an estimate depends on the uncertainty on model predictions, which in principle can be estimated from the spread in the presupernova neutrino number luminosity from different models in the current literature that begin with the same ZAMS. Unfortunately, the presupernova models in the present literature do not allow a reasonable direct comparison due to key, yet often undisclosed, modeling choices made during the evolution of a stellar model (although see Patton et al. 2017b for an exception). For example, the neutrino number luminosity can change by more than an order of magnitude due to the prescription used for mass loss by stellar winds over the evolution of the model, the treatment of convective boundaries, the spatial (mass) and temporal resolution of the model over its evolution, the global conservation of energy by the model over its evolution, the number of isotopes evolved by the nuclear reaction network, and how nuclear burning is coupled to the hydrodynamics (operator split versus fully coupled versus postprocessing) especially during the advanced stages of massive star evolution. We must conclude, therefore, that the idea to use models to place distance constraints will become realistic only in the future, after more progress is achieved on presupernova emission models.

5. Discussion

We have demonstrated that it will be possible to use the neutrino IBD signal at a large liquid scintillator detector to obtain an early localization of a nearby presupernova ($D\lesssim 1$ kpc). The method we propose is robust, as it has been used successfully for reactor neutrinos, and it is sufficiently simple that it can be implemented during a presupernova signal detection. For a detector where the forward–backward asymmetry is about 10% (realistic for JUNO), and 200 events detected (also realistic at JUNO, for a star like Betelgeuse) the angular resolution is $\beta \simeq 60^\circ$, which is moderate, but sufficient to exclude a large number of potential candidate progenitors.

The method has the potential to become even more sensitive if it is used with LS-Li, and therefore it provides further motivation to develop new experimental concepts in this direction. For example, 200 signal events with forward—backward asymmetry of $\sim\!40\%$ would result in a resolution of about 15°, and the possibility to uniquely identify the progenitor star.

In a realistic situation, as soon as a presupernova signal is detected with high confidence (a few tens of candidate events), an alert with coarse localization information can be issued, followed by updates with improved angular resolution in the minutes or hours leading to the neutrino burst detection.

Using the Patton et al. (2017b) presupernova model, we find that (see Figure 8) when the number of events reaches N=100 ($\simeq 1$ hr precollapse for Betelgeuse), the angular information is already close to optimal, since only a minimal improvement of the positional estimate can be gained at subsequent times. Note,

however, that our results are conservative. According to other simulations where the presupernova neutrino luminosity reaches a detectable level over a timescale of days (Kato et al. 2015; Guo et al. 2019), it might be possible to detect a larger number of events, resulting in even better angular resolutions in the last 1–2 hr before the core collapse.

It is possible that, when a nearby star reaches its final day or hours before becoming a supernova, a new array of neutrino detectors will be available. A large liquid scintillator experiment like the proposed THEIA (Askins et al. 2019), which could reach 80 kt (fiducial) mass, could observe more than 10³ IBD events, with an angular resolution of at least $\sim 30^{\circ}$. The resolution of THEIA would be improved by using a waterbased liquid scintillator, where the capability to separate the scintillation and Cerenkov light would result in enhanced pointing ability (e.g., Askins et al. 2019) for IBD, and in the possibility to use neutrino-electron elastic scattering for pointing. A subdominant, but still useful, contribution to the pointing effort—at the level of tens of events—will come from $\mathcal{O}(1)$ kt liquid scintillator projects like SNO+ (Andringa et al. 2016) and the Jinping Neutrino Experiment (Beacom et al. 2017), for which the deep underground depth will result in very low background levels. Further activities on directionality in scintillators are ongoing (e.g., Biller et al. 2020). Data from elastic scattering events at water Cerenkov detectors like SuperKamiokande (Simpson et al. 2019) and possibly the planned HyperKamiokande ($\mathcal{O}(100)$ kt) (Abe et al. 2016), will also contribute, despite the loss of statistics (compared to liquid scintillator) due to the higher energy threshold (\sim 5–7 MeV). In these detectors, a possible phase with Gadolinium dissolved in the water, like in the upcoming SuperK-Gd (Beacom & Vagins 2004; Simpson et al. 2019), will allow better discrimination of the IBD events, resulting in an enhanced pointing potential.

In addition to new experimental scenarios, a different theoretical panorama may be realized as well, and there might be novel avenues to conduct fundamental science tests (e.g., searches for exotic light and weakly interacting particles) using presupernova neutrinos.

We are grateful to S. Borthakur and L. M. Thomas for fruitful discussions. We acknowledge funding from the National Science Foundation grant No. PHY-1613708. This research was also supported at ASU by the NSF under grant PHY-1430152 for the Physics Frontier Center "Joint Institute for Nuclear AstrophysicsCenter for the Evolution of the Elements" (JINA-CEE). This research made extensive use of the SIMBAD Astronomical Database and SAO/NASA Astrophysics Data System (ADS).

Software: matplotlib (Hunter 2007), NumPy (van der Walt et al. 2011), and Wolfram Mathematica version 12.0.

Appendix Presupernova Candidates

Table A1 compiles a list of 31 red and blue core collapse supernova progenitors within 1 kpc that have both distance and mass estimates. Table A1 gives the star number (sorted by distance), Henry Draper (HD) catalog number, common name, constellation, distance, mass, J2000 right ascension (R.A.) and

J2000 declination (decl.). For stars with multiple distance measurements, precedence is given to distances provided by the Gaia Collaboration et al. (2018), van Leeuwen (2007), and individual determinations, in this order. Earlier compilations (e.g., Nakamura et al. 2016) considered only red supergiant progenitors and did not require a mass estimate.

Table A2 lists the angular distance $\Delta\theta$ of each star to its nearest neighbor. Table A2 gives the star number, HD catalog

Table A1Candidate Presupernova Stars

N	Catalog Name	Common Name	Constellation	Distance (kpc)	Mass (M_{\odot})	R.A.	Decl.
1	HD 116658	Spica/α Virginis	Virgo	0.077 ± 0.004^{a}	11.43 ^{+1.15} _{-1.15} b	13:25:11.58	-11:09:40.8
2	HD 149757	ζ Ophiuchi	Ophiuchus	0.112 ± 0.002^{a}	20.0°	16:37:09.54	-10:34:01.53
3	HD 129056	α Lupi	Lupus	0.143 ± 0.003^{a}	$10.1^{+1.0}_{-1.0}$ d	14:41:55.76	-47:23:17.52
4	HD 78647	λ Velorum	Vela	0.167 ± 0.003^{a}	$7.0^{+1.5e}_{-1.0}$	09:07:59.76	-43:25:57.3
5	HD 148478	Antares/ α Scorpii	Scorpius	$0.169 \pm 0.030^{\mathrm{a}}$	$11.0 - 14.3^{f}$	16:29:24.46	-26:25:55.2
6	HD 206778	ϵ Pegasi	Pegasus	0.211 ± 0.006^{a}	$11.7^{+0.8}_{-0.8}$	21:44:11.16	+09:52:30.0
7	HD 39801	Betelgeuse/ α Orionis	Orion	$0.222 \pm 0.040^{\rm r}$	$11.6^{+5.0\mathrm{g}}_{-3.9}$	05:55:10.31	+07:24:25.4
8	HD 89388	q Car/V337 Car	Carina	$0.230 \pm 0.020^{\mathrm{p}}$	$6.9^{+0.6d}_{-0.6}$	10:17:04.98	-61:19:56.3
9	HD 210745	ζ Cephei	Cepheus	$0.256 \pm 0.006^{\mathrm{p}}$	$10.1^{+0.1d}_{-0.1}$	22:10:51.28	+58:12:04.5
10	HD 34085	Rigel/ β Orion	Orion	0.264 ± 0.024^{a}	$21.0^{+3.0h}_{-3.0}$	05:14:32.27	-08:12:05.90
11	HD 200905	ξ Cygni	Cygnus	$0.278 \pm 0.029^{\rm p}$	8.0 ⁱ	21:04:55.86	+43:55:40.3
12	HD 47839	S Monocerotis A	Monoceros	0.282 ± 0.040^{a}	29.1 ^j	06:40:58.66	+09:53:44.71
13	HD 47839	S Monocerotis B	Monoceros	0.282 ± 0.040^{a}	21.3 ^j	06:40:58.57	+09:53:42.20
14	HD 93070	w Car/V520 Car	Carina	$0.294 \pm 0.023^{\mathrm{p}}$	$7.9^{+0.1d}_{-0.1}$	10:43:32.29	-60:33:59.8
15	HD 68553	NS Puppis	Puppis	0.321 ± 0.032^{p}	9.7 ^d	08:11:21.49	-39:37:06.8
16	HD 36389	CE Tauri/119 Tauri	Taurus	$0.326 \pm 0.070^{\mathrm{p}}$	14.37 ^{+2.00k}	05:32:12.75	+18:35:39.2
17	HD 68273	γ^2 Velorum	Vela	0.342 ± 0.035^{a}	$9.0^{+0.61}_{-0.6}$	08:09:31.95	-47:20:11.71
18	HD 50877	o ¹ Canis Majoris	Canis Major	$0.394 \pm 0.052^{\mathrm{p}}$	$7.83^{+2.0}_{-2.0}$ d	06:54:07.95	-24:11:03.2
19	HD 207089	12 Pegasi	Pegasus	$0.415 \pm 0.031^{\mathrm{p}}$	$6.3^{+0.7}_{-0.7}$	21:46:04.36	+22:56:56.0
20	HD 213310	5 Lacertae	Lacerta	0.505 ± 0.046^{a}	$5.11^{+0.18}_{-0.18}$	22:29:31.82	+47:42:24.8
21	HD 52877	σ Canis Majoris	Canis Major	0.513 ± 0.108^{p}	$12.3^{+0.1d}_{-0.1}$	07:01:43.15	-27:56:05.4
22	HD 208816	VV Cephei	Cepheus	$0.599 \pm 0.083^{\mathrm{p}}$	$10.6^{+1.0}_{-1.0}$	21:56:39.14	+63:37:32.0
23	HD 196725	θ Delphini	Delphinus	$0.629 \pm 0.029^{\rm p}$	$5.60^{+3.0}_{-3.0}$	20:38:43.99	+13:18:54.4
24	HD 203338	V381 Cephei	Cepheus	0.631 ± 0.086^{p}	12.0°	21:19:15.69	+58:37:24.6
25	HD 216946	V424 Lacertae	Lacerta	$0.634 \pm 0.075^{\mathrm{p}}$	$6.8^{+1.0}_{-1.0}$ q	22:56:26.00	+49:44:00.8
26	HD 17958	HR 861	Cassiopeia	$0.639 \pm 0.039^{\mathrm{p}}$	$9.2^{+0.5}_{-0.5}$ d	02:56:24.65	+64:19:56.8
27	HD 80108	HR 3692	Vela	$0.650 \pm 0.061^{\text{p}}$	$12.1^{+0.2}_{-0.2}$ d	09:16:23.03	-44:15:56.6
28	HD 56577	145 Canis Major	Canis Major	$0.697 \pm 0.078^{\mathrm{p}}$	$7.8^{+0.5}_{-0.5}$ d	07:16:36.83	-23:18:56.1
29	HD 219978	V809 Cassiopeia	Cassiopeia	$0.730 \pm 0.074^{\rm p}$	$8.3^{+0.5d}_{-0.5}$	23:19:23.77	+62:44:23.2
30	HD 205349	HR 8248	Cygnus	$0.746 \pm 0.039^{\rm p}$	$6.3^{+0.7}_{-0.7}$ d	21:33:17.88	+45:51:14.5
31	HD 102098	Deneb/α Cygni	Cygnus	$0.802 \pm 0.066^{\rm s}$	$19.0^{+4.0}_{-4.0}$ s	20:41:25.9	+45:16:49.0

Notes.

^a van Leeuwen (2007).

^b Tkachenko et al. (2016).

^c Howarth & Smith (2001).

^d Tetzlaff et al. (2011).

e Carpenter et al. (1999).

f Ohnaka et al. (2013).

g Neilson et al. (2011).

^h Shultz et al. (2014).

i Reimers & Schroeder (1989).

Cvetkovic et al. (2009).

^k Montargès et al. (2018).

¹ North et al. (2007).

^m Baines et al. (2018).

ⁿ van Belle et al. (2009), Malagnini et al. (2000).

^o Tokovinin (1997)

^p Gaia Collaboration et al. (2018).

^q Lee et al. (2014).

r Harper et al. (2017).

^s Schiller & Przybilla (2008).

Table A2
Minimum Angular Separation between Presupernova Candidates

N	Catalog/Common Name	Min. Ang. Separation (deg)	Nearest Neighbor Name	Nearest Neighbor Number
1	HD 116658/Spica	39.66	HD 129056/α Lupi	3
2	HD 149757/ζ Ophiuchi	15.97	HD 148478/Antares	5
3	HD 129056/ α Lupi	29.73	HD 148478/Antares	5
4	HD $78647/\lambda$ Velorum	1.73	HD 80108/HR 3692	27
5	HD 148478/Antares	15.97	HD 149757/ ζ Ophiuchi	2
6	HD 206778/ ϵ Pegasi	13.08	HD 207089/12 Pegasi	19
7	HD 39801/Betelgeuse	11.59	S Mono A/B	12/13
8	HD 89338/q Car	3.30	HD 93070/w Car	14
9	HD 210745/ ζ Cephei	5.69	HD 208816/VV Cephei	22
10	HD 34085/Rigel	18.60	HD 39801/Betelgeuse	7
11	HD $200905/\zeta$ Cygni	4.39	HD 102098/Deneb	31
12	HD 47839/S Mono A	11.60	HD 39801/Betelgeuse	7
13	HD 47839/S Mono B	11.60	HD 39801/Betelgeuse	7
14	HD 93070/w Car	3.30	HD 89338/q Car	8
15	HD 68553/NS Puppis	7.72	HD $68273/\gamma^2$ Velorum	17
16	HD 36389/119 Tauri	12.50	HD 39801/Betelgeuse	7
17	HD $68273/\gamma^2$ Velorum	7.72	HD 68553/NS Puppis	15
18	HD 50877/o ¹ Canis Majoris	4.12	HD 52877/ σ Canis Majoris	21
19	HD 207089/12 Pegasi	13.08	HD 206778/ ϵ Pegasi	6
20	HD 213310/5 Lacertae	4.88	HD 216946/V424 Lacertae	25
21	HD $52877/\sigma$ Canis Majoris	4.12	HD 50877/o ¹ Canis Majoris	18
22	HD 208816/VV Cephei	5.69	HD $210745/\zeta$ Cephei	9
23	HD $196725/\theta$ Delphini	16.39	HD 206778/ ϵ Pegasi	6
24	HD 203338/V381 Cephei	6.72	HD 208816/VV Cephei	22
25	HD 216946/V424 Lacertae	4.88	HD 213310/5 Lacertae	20
26	HD 17958/HR 861	23.49	HD 219978/V809 Cassiopeia	29
27	HD 80108/HR 3692	1.73	HD 78647/ λ Velorum	4
28	HD 56577/145 Canis Majoris	5.22	HD $50877/o^1$ Canis Majoris	18
29	HD 219978/V809 Cassiopeia	9.33	HD 208816/VV Cephei	22
30	HD 205349/HR 8248	5.38	HD $200905/\zeta$ Cygni	11
31	HD 102098/Deneb	4.39	HD $200905/\zeta$ Cygni	11

and common name, the minimum angular separation between the star and its nearest neighbor, the HD catalog and common name of the nearest neighbor, and the star number of the nearest neighbor. The R.A. and decl. for each star is taken from Table A1 when calculating angular separations.

ORCID iDs

Mainak Mukhopadhyay https://orcid.org/0000-0002-2109-5315

Cecilia Lunardini https://orcid.org/0000-0002-9253-1663
F. X. Timmes https://orcid.org/0000-0002-0474-159X
Kai Zuber https://orcid.org/0000-0001-8689-4495

References

Aalbers, J., Agostini, F., Alfonsi, M., et al. 2016, JCAP, 2016, 017
Aalseth, C. E., Acerbi, F., Agnes, P., et al. 2018, EPJP, 133, 131
Abe, K., Haga, Y., Hayato, Y., et al. 2016, APh, 81, 39
Acciarri, R., Acero, M. A., Adamowski, M., et al. 2016, arXiv:1601.02984
Alekseev, E. N., Alekseeva, L. N., Volchenko, V. I., & Krivosheina, I. V. 1987, JETPL, 45, 589
An, F., An, G., An, Q., et al. 2016, JPhG, 43, 030401
Andringa, S., Arushanova, E., Asahi, S., et al. 2016, AdHEP, 2016, 6194250
Antonioli, P., Tresch Fienberg, R., Fleurot, R., et al. 2004, NJPh, 6, 114
Apollonio, M., Baldini, A., Bemporad, C., et al. 2000, PhRvD, 61, 012001
Araki, T., Eguchi, K., Enomoto, S., et al. 2005, PhRvL, 94, 081801
Asakura, K., Gando, A., Gando, Y., et al. 2016, ApJ, 818, 91
Askins, M., Bagdasarian, Z., Barros, N., et al. 2019, EPJC, 80, 416

```
Baines, E. K., Armstrong, J. T., Schmitt, H. R., et al. 2018, AJ, 155, 30
Beacom, J. F., Chen, S., Cheng, J., et al. 2017, ChPhC, C41, 023002
Beacom, J. F., & Vagins, M. R. 2004, PhRvL, 93, 171101
Beacom, J. F., & Vogel, P. 1999, PhRvD, 60, 033007
Beaudet, G., Petrosian, V., & Salpeter, E. E. 1967, ApJ, 150, 979
Biller, S. D., Leming, E. J., & Paton, J. L. 2020, NIMPA, 972, 164106
Bionta, R. M., Blewitt, G., Bratton, C. B., et al. 1987, PhRvL, 58, 1494
Bisnovatyi-Kogan, G. S., & Seidov, Z. F. 1984, NYASA, 422, 319
Borexino Collaboration, Agostini, M., Altenmüller, K., et al. 2018, Natur,
  562, 505
Brugière, T. 2017, NIMPA, 845, 326
Cao, L. J., & Wang, Y. 2017, ARNPS, 67, 183
Carpenter, K. G., Robinson, R. D., Harper, G. M., et al. 1999, ApJ, 521, 382
Cvetkovic, Z., Vince, I., & Ninkovic, S. 2009, POBeo, 86, 331
Daya Bay Collaboration, Guo, X., Wang, N., et al. 2007, arXiv:hep-ex/
  0701029
Farag, E., Timmes, F. X., Taylor, M., Patton, K. M., & Farmer, R. 2020, ApJ,
  893, 133
Fischer, V., Chirac, T., Lasserre, T., et al. 2015, JCAP, 2015, 032
Fowler, W. A., & Hoyle, F. 1964, ApJS, 9, 201
Fuller, G. M., Fowler, W. A., & Newman, M. J. 1980, ApJS, 42, 447
Fuller, G. M., Fowler, W. A., & Newman, M. J. 1982a, ApJS, 48, 279
Fuller, G. M., Fowler, W. A., & Newman, M. J. 1982b, ApJ, 252, 715
Fuller, G. M., Fowler, W. A., & Newman, M. J. 1985, ApJ, 293, 1
Gaia Collaboration, Brown, A. G. A., Vallenari, A., et al. 2018, A&A, 616, A1
Großschedl, J. E., Alves, J., Teixeira, P. S., et al. 2019, A&A, 622, A149
Guo, G., Qian, Y.-Z., & Heger, A. 2019, PhLB, B796, 126
Harper, G. M., Brown, A., Guinan, E. F., et al. 2017, AJ, 154, 11
Hirata, K., Kajita, T., Koshiba, M., Nakahata, M., & Oyama, Y. 1987, PhRvL,
  58, 1490
Hirata, K. S., Kajita, T., Koshiba, M., et al. 1988, PhRvD, 38, 448
Howarth, I. D., & Smith, K. C. 2001, MNRAS, 327, 353
```

```
Hunter, J. D. 2007, CSE, 9, 90
IceCube Collaboration, Aartsen, M. G., Ackermann, M., et al. 2018a, Sci, 361,
   eaat1378
IceCube Collaboration, Aartsen, M. G., Ackermann, M., et al. 2018b, Sci,
  361, 147
Itoh, N., Hayashi, H., Nishikawa, A., & Kohyama, Y. 1996, ApJS, 102, 411
Kato, C., Delfan Azari, M., Yamada, S., et al. 2015, ApJ, 808, 168
Kato, C., Nagakura, H., Furusawa, S., et al. 2017, ApJ, 848, 48
Krauss, L. M., Glashow, S. L., & Schramm, D. N. 1984, Natur, 310, 191
Kutschera, M., Odrzywołek, A., & Misiaszek, M. 2009, AcPPB, 40, 3063
Kyutoku, K., & Kashiyama, K. 2018, PhRvD, 97, 103001
Langanke, K., & Martínez-Pinedo, G. 2000, NuPhA, 673, 481
Langanke, K., & Martínez-Pinedo, G. 2014, NuPhA, 928, 305
Lee, B. C., Han, I., Park, M. G., Hatzes, A. P., & Kim, K. M. 2014, A&A,
   566, A124
Li, H.-L., Li, Y.-F., Wen, L.-J., & Zhou, S. 2020, JCAP, 05, 049
Li, Y.-F. 2014, IJMPS, 31, 1460300
Lim, B., Nazé, Y., Gosset, E., & Rauw, G. 2019, MNRAS, 490, 440
Lin, Z., & Lunardini, C. 2020, PhRvD, 101, 023016
Malagnini, M. L., Morossi, C., Buzzoni, A., & Chavez, M. 2000, PASP,
   112, 1455
Misch, G. W., Sun, Y., & Fuller, G. M. 2018, ApJ, 852, 43
Montargès, M., Norris, R., Chiavassa, A., et al. 2018, A&A, 614, A12
Nakamura, K., Horiuchi, S., Tanaka, M., et al. 2016, MNRAS, 461, 3296
Neilson, H. R., Lester, J. B., & Haubois, X. 2011, in ASP Conf. Ser. 451, 9th
   Pacific Rim Conference on Stellar Astrophysics, ed. S. Qain et al. (San
   Francisco, CA: ASP), 117
Newstead, J. L., Strigari, L. E., & Lang, R. F. 2019, PhRvD, 99, 043006
```

```
North, J. R., Tuthill, P. G., Tango, W. J., & Davis, J. 2007, MNRAS, 377, 415
Odrzywolek, A. 2009, PhRvC, 80, 045801
Odrzywolek, A., Misiaszek, M., & Kutschera, M. 2004a, APh, 21, 303
Odrzywolek, A., Misiaszek, M., & Kutschera, M. 2004b, AcPPB, B35, 1981
Ohnaka, K., Hofmann, K. H., Schertl, D., et al. 2013, A&A, 555, A24
Patton, K. M., Lunardini, C., & Farmer, R. J. 2017a, ApJ, 840, 2
Patton, K. M., Lunardini, C., Farmer, R. J., & Timmes, F. X. 2017b, ApJ, 851, 6
Patton, K. M., Lunardini, C., Farmer, R. J., & Timmes, F. X. 2019, Neutrinos
   from Beta Processes in a Presupernova: Probing the Isotopic Evolution of a
  Massive Star v1, Zenodo, doi:10.5281/zenodo.2626645
Raffelt, G. G., Redondo, J., & Viaux Maira, N. 2011, PhRvD, 84, 103008
Raj, N., Takhistov, V., & Witte, S. J. 2020, PhRvD, 101, 043008
Reimers, D., & Schroeder, K. P. 1989, A&A, 214, 261
Schiller, F., & Przybilla, N. 2008, A&A, 479, 849
Schinder, P. J., Schramm, D. N., Wiita, P. J., Margolis, S. H., & Tubbs, D. L.
   1987, ApJ, 313, 531
Shultz, M., Wade, G. A., Petit, V., et al. 2014, MNRAS, 438, 1114
Simpson, C., Abe, K., Bronner, C., et al. 2019, ApJ, 885, 133
Tanaka, H. K. M., & Watanabe, H. 2014, NatSR, 4, 4708
Tetzlaff, N., Neuhäuser, R., & Hohle, M. M. 2011, MNRAS, 410, 190
Tkachenko, A., Matthews, J. M., Aerts, C., et al. 2016, MNRAS, 458, 1964
Tokovinin, A. A. 1997, A&AS, 124, 75
van Belle, G. T., Creech-Eakman, M. J., & Hart, A. 2009, MNRAS, 394, 1925
van der Walt, S., Colbert, S. C., & Varoquaux, G. 2011, CSE, 13, 22
van Leeuwen, F. 2007, A&A, 474, 653
Vogel, P., & Beacom, J. F. 1999, PhRvD, 60, 053003
Yoshida, T., Takahashi, K., Umeda, H., & Ishidoshiro, K. 2016, PhRvD, 93,
   123012
```